Bipolar spin-conversion diode and quantum entanglement induced by the valley and pseudoparity mixing

Mengyao Li,[1] Ning Bu,[1] Jingguo Hu,[3] Yongchun Tao,[1,*] Hao Fu,[1,2,†] and Jun Wang[4,‡]

[1]*Department of Physics, Nanjing Normal University, Nanjing 210023, China*
[2]*School of Mathematical Sciences, Nanjing Normal University, Nanjing, 210023, China*
[3]*Department of Physics, Yangzhou University, Yangzhou 225009, China*
[4]*Department of Physics, Southeast University, Nanjing 210096, China*

(Received 16 July 2022; revised 7 October 2022; accepted 10 October 2022; published 4 November 2022)

Herein, we report on a zigzag graphene superconducting junction with a superconductor sandwiched in between two magnetized zigzag graphene nanoribbons, where the valley and pseudoparity mixing are shown to bring about peculiar properties. We find that the bipolar spin diode and spin-conversion diode in the ferromagnetic configuration as well as quantum entanglement in the antiferromagnetic one are exhibited. The noncollinear angle combined with the valley and pseudoparity mixing in arbitrary magnetic configurations exerts a significant influence on the transport properties. In addition, not only the bipolar spin diode and magnetic storage with high efficiencies but also the bipolar spin-conversion diode and quantum entanglement can coexist in one setup. Particularly, the bipolar spin-conversion diode can be used to directly detect and confirm the helical spin texture of the edge state in a quantum spin Hall insulator.

DOI: 10.1103/PhysRevResearch.4.043078

I. INTRODUCTION

In recent years, the emergence of new materials, graphene and typically graphenelike monolayers, including silicene, germanene, and stanene, has brought a new perspective to spintronics and valleytronics [1–17]. In these two-dimensional materials, the two valleys at the K and K' points of the Brillouin zone characterized by a pseudo-spin degree of freedom, are related to each other by time-reversal symmetry like the spin degree of freedom. Thus a superconducting Cooper pair should be composed of electrons from the two opposite valley bands, which is also the key mechanism in valley-based superconducting spintronics. Particularly, for a zigzag graphene nanoribbon (ZR) with even-number chain, the electron wave function has odd or even pseudoparity. The electrons are only allowed to transport between the same pseudoparity bands by the valley-selection rule [1–5].

The superconducting junctions based on the ZRs have been extensively studied [18–23], for instance, the nonlocal quantum transport properties of a graphene superconducting spin valve. In this spin valve, for all bias voltages, a spin-switch effect between perfect crossed Andreev reflection (CAR) and perfect elastic cotunneling (EC) in the low-energy regime by reversing the magnetization direction in one of the ferromagnetic layers, has been exhibited [23]. However, the report on the interplay between the magnetic configuration and pseudoparity of the particle in magnetized ZR (MZR) lacks enough. In particular, due to the electrons or holes having no valley degree in the bulk SC, the valley and pseudoparity mixing at the interface between the ZR and bulk superconductor (SC) are induced, which are favor of enriching the superconducting spintronic properties. Owing to the mixing, many important superconducting spintronic applications, such as the spin filtering for spin diode [24–29] and quantum entanglement [30–41], are exhibited, as shown in the following parts. Therefore it is urgent to study such magnetic superconducting junctions based on the two MZRs.

In this work, using a Green's function method, we investigate a zigzag graphene superconducting junction with two MZRs directly coupled to the SC layer, which is different from the situation of the graphene superconducting spin valve [23]. Due to the valley and pseudoparity mixing, novel features for the Andreev reflection (AR), EC, and CAR processes in different magnetic configures, are exhibited. It is shown that for the ferromagnetic (F) configuration, with increasing exchange energy, there can only exist EC process for certain spin or with conversion from certain spin to the opposite one irrespective of the bias voltage polarities. This can be applied to manufacture the bipolar spin diode and bipolar spin-conversion diode. In the antiferromagnetic (AF) configuration, at a small SC length, all scattering processes are basically depressed, thus the system can be used to design the magnetic storage device of high efficiency. However, under a big SC length, there can be only CAR process for spin up or down regardless of the exchange energy, indicating the perfect quantum entanglement. Furthermore, the noncollinear angle

*yctao88@163.com
†161002003@njnu.edu.cn
‡jwang@seu.edu.cn

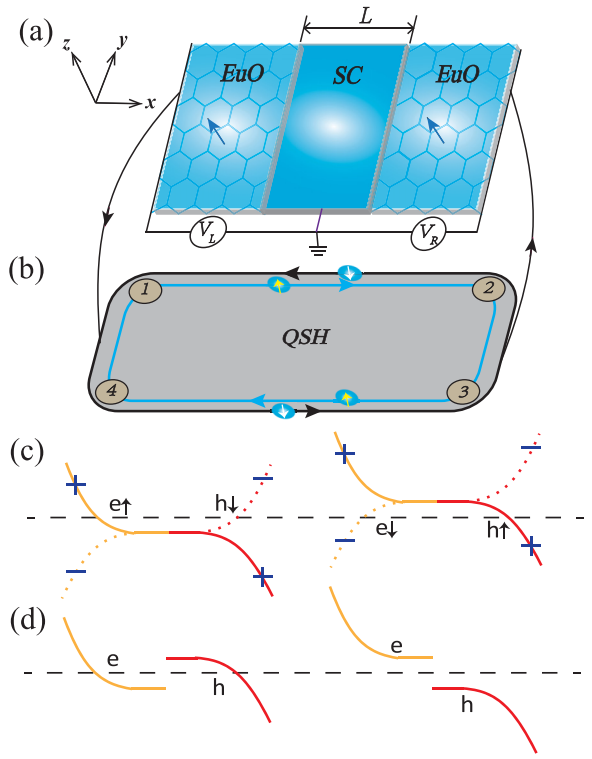

FIG. 1. (a) A grounded s-wave SC lead of length L is sandwiched in between the left and right MZR leads applied with voltage V_L and V_R, respectively, which can be realized by the ferromagnetic proximity. Here, two ferromagnetic insulators such as EuO magnetized by the magnetic field **H**, are respectively placed on the left and right ZRs. (b) The QSH insulator is sketched, where the blue and black lines illustrate the helical edge states with the vertical arrows representing the spin orientation. (c) The electron and hole energy dispersions of the edge states in a magnetized even ZR with the gate voltages $U_{L(R)} = 0$, where the hole band "h" is obtained as a mirror image of the electron band "e" over the Fermi level (horizontal dotted line) with "+" and "−" denoting the even and odd pseudoparities of the edgestates, respectively. In addition, the spin-up (-down) electron band overlaps with spin-down (-up) hole band of opposite pseudoparities, and the spin exchange energy causes a shift of the Dirac point from the Fermi level. (d) The corresponding energy dispersions for the situation of the bulk SC with the left (the gate voltage $U_S > 0$) and right ($U_S < 0$) panels.

in arbitrary magnetic configurations has a significant effect on the transport properties. In particular, the present structure can be combined with the quantum spin Hall (QSH), so that we would present a unambiguous evidence of the helical spin texture being still lacking [42–49].

II. MODEL WITH THE VALLEY AND PSEUDOPARITY MIXING INDUCED BY THE BULK SC

Consider an MZR/SC/MZR junction shown in Fig. 1, where an s-wave SC metal is grounded, the length of SC region is La with a the lattice constant, the left and right MZRs are respectively biased V_L and V_R, and the width of the ribbon is given by the zigzag chain number N. We utilize the following Hamiltonian [5] to describe the structure

$$\begin{aligned} H =& \sum_{l\sigma} (U_j + \boldsymbol{h}\cdot\boldsymbol{\sigma}) C^\dagger_{l\sigma} C_{l\sigma} - \sum_{\langle lm\rangle} t (C^\dagger_{l\sigma} C_{m\sigma} + \text{c.c.}) \\ &+ \sum_{k\sigma} (\varepsilon_k - U_S) b^\dagger_{k\sigma} b_{k\sigma} \\ &+ \sum_{k} (\Delta b^\dagger_{k\uparrow} b^\dagger_{-k\downarrow} + \text{c.c.}) + \sum_{\langle li\rangle\sigma} (t_{li} C^\dagger_{l\sigma} b_{i\sigma} + \text{c.c.}), \end{aligned} \quad (1)$$

where the first and second terms describe the two MZRs with $C^\dagger_{l\sigma}(C_{l\sigma})$ the creation (annihilation) operator at site l with spin $\sigma(\sigma = \pm = \uparrow\downarrow)$, U_j the lattice site energies of the left ($j = L$) and right ($j = R$) ribbon regions, $\boldsymbol{h}\cdot\boldsymbol{\sigma}$ the spin exchange term induced by magnetic proximity, $\langle lm\rangle$ denoting the summation over the nearest neighbor sites, and $t = 2.8$ eV the hopping integral; the third and fourth terms describe the SC metal lead with U_S the chemical potential and Δ the superconducting pair potential. The last term is the coupling between the bulk SC furface and the two MZR ribbons with t_{li} the hoping energy and $b_{i\sigma}$ the lattice version of the operator $b_{k\sigma}$ in the SC region, where the surface connecting the two MZRs can be regarded a ribbon. The exchange fields of the two MZRs are respectively assumed to be $\boldsymbol{h}_L = (0, 0, h)$ and $\boldsymbol{h}_R = (h\sin\theta, 0, h\cos\theta)$, which corresponds to the F (AF) configuration with $\theta = 0\,(\pi)$ and the arbitrary one with $\theta \neq 0$ and π.

The device in Fig. 1(a) can be deemed as a three-terminal device in which the left MZR, right MZR, and SC metal leads are connected to the SC ribbon region. In the left MZR lead, the current can be obtained from the standard Keldysh formalism

$$I_L = \frac{e}{h}\int dE\ Tr[H_{i,i+1}G^<_{i,i+1}(E) - G^<_{i,i+1}(E)H_{i+1,i}]_{ee}, \quad (2)$$

where $H_{i,i+1}$ refers to the hopping matrix between two neighboring slices of the MZR with i a unit slice index, $G^<$ denotes the lesser Green's function defined as in the Appendix A, the trace is performed over the transverse site and spin space, and the subscript ee represents the electron component for the Nambu space.

In the light of the Keldysh formula $G^< = G^r\Sigma^< G^a$ with $G^{r(a)}$ the retarded (advanced) Green's function and $\Sigma^<$ the lesser self-energy, the current is reduced to

$$\begin{aligned} I_L = \frac{e}{h}\int dE\ Tr\big\{&\Gamma^L_{ee} G^r_{ee} \Gamma^R_{ee} G^a_{ee}(f_L - f_R) \\ &+ \Gamma^L_{ee} G^r_{eh} \Gamma^L_{hh} G^a_{he}(f_L - \bar{f}_L) \\ &+ \Gamma^L_{ee} G^r_{eh} \Gamma^R_{hh} G^a_{he}(f_L - \bar{f}_R) + \Gamma^L_{ee} G^r \Gamma^S G^a (f_L - f_S)\big\}, \end{aligned} \quad (3)$$

where the four terms respectively describe the EC, local AR, CAR, and quasiparticle's tunneling processes, and the last one occurs mainly out of the superconducting energy gap. In Eq. (3), f_j ($j = L, R, S$) stands for the Fermi-Dirac distribution function in the jth lead with $f_{L(R)} = f(E + eV_{L(R)})$ and $\bar{f}_{L(R)} = f(E - eV_{L(R)})$, and $\Gamma^j = i(\Sigma^{jr} - \Sigma^{ja})$ denotes the linewidth function of the jth lead with $\Sigma^r = [\Sigma^a]^\dagger$ the self-energy.

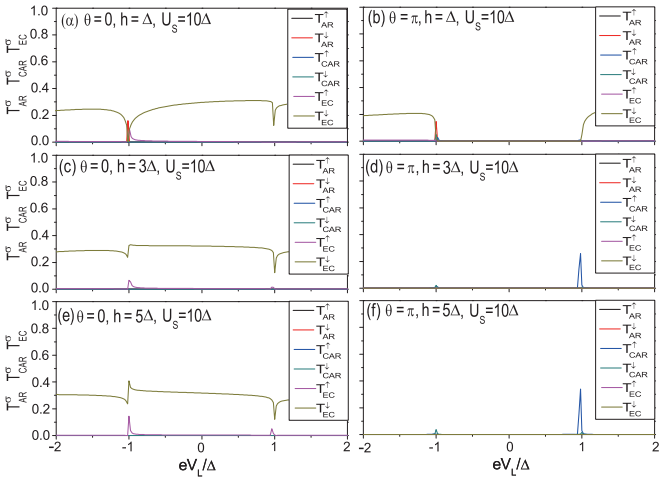

FIG. 2. The spin-up and spin-down AR, CAR and EC transmission probabilities for the F (the left column) and AF (the right column) configurations vs eV_L. Here, $L = 40$, $eV_R = 0$, $U_L = U_R = 0$, $U_S = 10\Delta$, $h = \Delta$ for (a) and (b), 3Δ for (c) and (d), and 5Δ for (e) and (f).

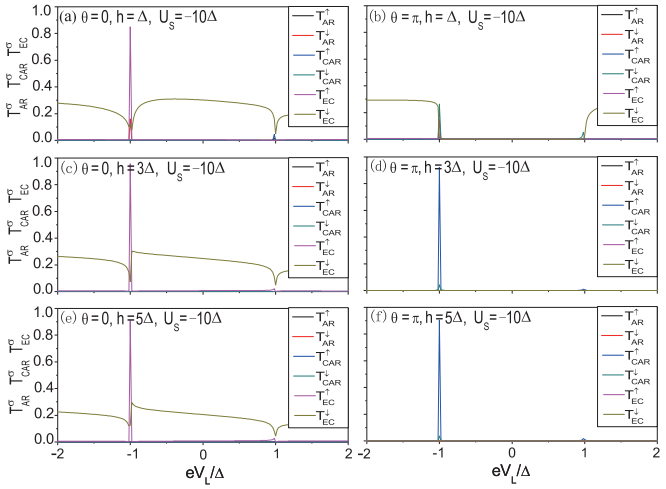

FIG. 3. The same as in Fig. 2 except for $U_S = -10\Delta$.

III. RESULTS AND DISCUSSIONS

In calculations, the zero temperature $T = 0$K is considered, the pair potential and linewidth constant of the SC lead are respectively set as $\Delta = 1$ meV and $g^S = 2\Delta$, $\Gamma^{L(R)}$ can be directly calculated from a semi-infinite MZR, and the zigzag chain number is taken to be even number 14.

A. The bias voltage combined with the exchange energy

Figure 2 illustrates the spin-resolved AR, CAR, and EC probabilities, respectively denoted by $T^{\sigma}_{\rm AR}$, $T^{\sigma}_{\rm CAR}$, and $T^{\sigma}_{\rm EC}$, which are as a function of the left bias voltage eV_L for the F and AF configurations with less increase of the exchange energy h at $U_S = 10\Delta$ and SC length $L = 40$. For the F configuration, the AR and CAR processes for the spin up and down both disappear, and the spin-up EC process also disappears nearly while only spin-down EC process remains. The less increase of h cannot bring about any changes of the features except for a slight change in the magnitude of $T^{\downarrow}_{\rm EC}$ for the spin-down EC process. Therefore the system can be used to manufacture the spin-filtering device on a large scale of negative and positive eV_L. For the AF configuration, it is found that at $|eV_L| < \Delta$, all the scattering processes for both spin up and down disappear, while at $|eV_L| > \Delta$, only spin-down EC process remains at small h as in the F configuration and no scattering process emerges at large h, which suggests a magnetic storage of high efficiency. All quantities, $T^{\sigma}_{\rm AR}$, $T^{\sigma}_{\rm CAR}$, and $T^{\sigma}_{\rm EC}$ at $U_S = -10\Delta$, are shown in Fig. 3, in which the corresponding features still remain except for a slight change of magnitude. Now we observe the situation for $L = 31$, as shown in Fig. 4. In the F configuration, in the range of $|eV_L| < \Delta$, there exists only the spin-up EC process ($T^{\uparrow}_{\rm EC} \neq 0$) at small h, which is thoroughly different from the situation for $L = 40$ only with $T^{\downarrow}_{\rm EC} \neq 0$. Particularly, with increasing h, $T^{\downarrow}_{\rm EC}$ starts to increase from 0 while $T^{\uparrow}_{\rm EC}$ decreases gradually. Beyond Δ for eV_L, with the increase of h, only $T^{\uparrow}_{\rm EC}$ keeps at negative eV_L but both $T^{\downarrow}_{\rm EC}$ and $T^{\uparrow}_{\rm EC}$ exist at positive eV_L, which is also different from the case at $L = 40$. In the AF configuration, at $|eV_L| < \Delta$, although there are $T^{\downarrow}_{\rm CAR}$ and $T^{\uparrow}_{\rm CAR}$, the former dies out with the enhancement of h. Nevertheless, at $|eV_L| > \Delta$, there are only small $T^{\uparrow}_{\rm EC}$ and $T^{\downarrow}_{\rm EC}$, which fall down to zero gradually with h. It follows that at $L = 31$, h exerts an influence on the $T^{\sigma}_{\rm EC}$ and $T^{\sigma}_{\rm CAR}$, so that we necessarily get insight into the effect of great increase of h on them. In Fig. 5, the probabilities for all processes as a function of eV_L with great increase of h are plotted. We notice that in the F configuration, on the scale of $|eV_L| < \Delta$, there is almost only spin-up EC process from $h = \Delta$, then spin-down EC process emerges, finally only spin-down EC process remains at $h = 40\Delta$. As a result, spin-up EC process can gradually evolve into spin-down one. In other words, with great increase of h, there exists the spin-current with the conversion from one spin direction to the other. Similarly, the feature also takes place at $|eV_L| > \Delta$, except that the magnitude is no more than slightly small. In the AF configuration, both $T^{\uparrow}_{\rm CAR}$ and $T^{\downarrow}_{\rm CAR}$ exist at $|eV_L| < \Delta$, but the former predominates. At $|eV_L| > \Delta$, both $T^{\downarrow}_{\rm EC}$ and $T^{\uparrow}_{\rm EC}$ for negative eV_L appear and the former similarly

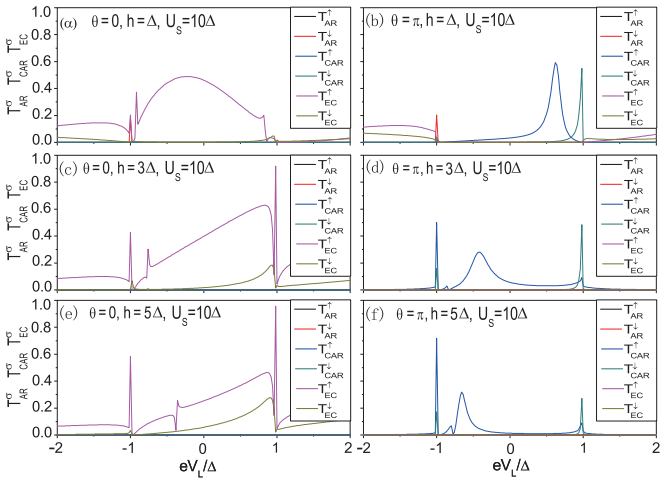

FIG. 4. The same as in Fig. 2 except for $L = 31$.

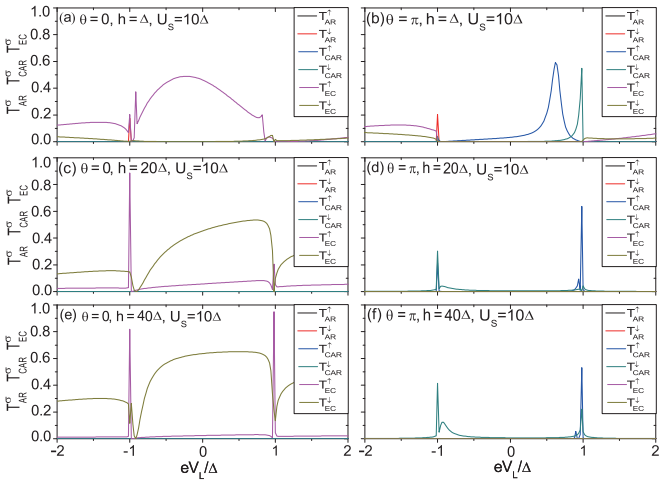

FIG. 5. The same as in Fig. 2 except that $L = 31$, $h = \Delta$ for (a) and (b), 20Δ for (c) and (d), and 40Δ for (e) and (f).

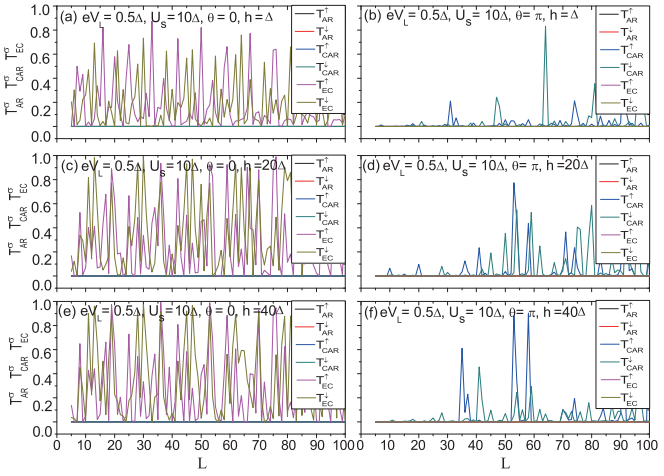

FIG. 7. The same as in Fig. 6 except that $h = \Delta$ for (a) and (b), 20Δ for (c) and (d), and 40Δ for (e) and (f).

reigns, whereas, although both of them for positive eV_L exist, they are too small. Particularly, at large h, all processes are suppressed. In addition, at $U_S = -10\Delta$, there exist the same features as those at $U_S = 10\Delta$, which are not plotted by figures for simplicity. From the above, it is concluded that there are thoroughly different features for different L, therefore, it is necessary for one to further investigate the effect of L.

B. The interplay between the SC length and spin exchange energy

The dependence of T^{σ}_{AR}, $T^{\sigma}_{\mathrm{CAR}}$, and T^{σ}_{EC} on the SC length L are illustrated in Fig. 6 for the F and AF configurations with less increase of h at $U_S = 10\Delta$. In the F configuration, there exist only EC processes for the spin up and down, which are shown to oscillate strongly and fast with L. The increase of h can change the values of the peaks and valleys but not their locations basically, and the peaks (valleys) for the spin up and down always do not overlap due to the exchange energy. In

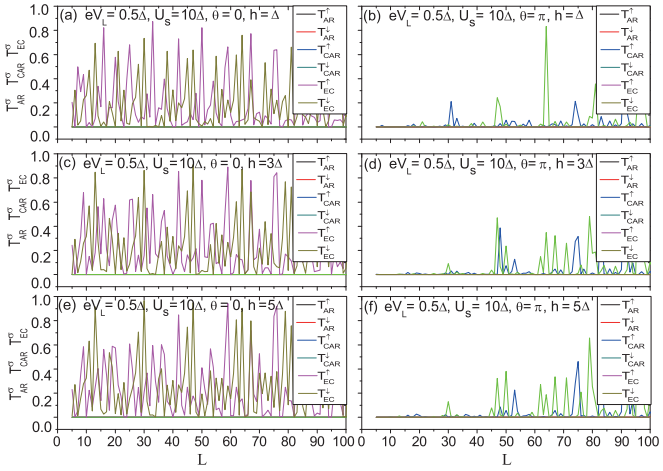

FIG. 6. The AR, CAR and EC probabilities for the F (the left column) and AF (the right column) configurations versus the SC region length L. Here, $eV_L = 0.5\Delta$, $U_L = U_R = 0$, $U_S = 10\Delta$, $h = \Delta$ for (a) and (b), 3Δ for (c) and (d), and 5Δ for (e) and (f).

the whole oscillation, the valley values of zero and nonzero both exist. There exists a wide of range for L, i.e., $L = 5$, 37, and 54 (6, 10, 23, 40, 57, and 78), at which the EC process for the spin up (down) remains while for the spin down (up) is thoroughly depressed. As discussed before for $L = 40$ (see the left column of Fig. 2), the spin filtering is also not varied with the bias voltage eV_L for these SC lengths, which can be used to manufacture bipolar spin diodes. In the AF configuration, there exist only $T^{\uparrow}_{\mathrm{CAR}}$ and $T^{\downarrow}_{\mathrm{CAR}}$, which oscillate weakly and slowly with L, particularly, are basically depressed at $L < 45$ with the increase of h. This means that during this scope, the spin filtering and magnetic storage with high efficiencies coexist in one setup, as shown in Fig. 2 for $L = 40$. More importantly, due to the interplay between L and h, the SC lengths L for the valleys of the CAR processes with the spin up and down are different. Therefore we can always find only CAR processes for some spin remaining with the increase of the exchange energy at certain SC length, which is just desirable. For instance, there are only CAR processes for spin up at $L = 74$ and 91, while for spin up at $L = 47$, 64, 81 and 96, which means that quantum entanglement is produced at these SC lengths. In Fig. 7, T^{σ}_{AR}, $T^{\sigma}_{\mathrm{CAR}}$, and T^{σ}_{EC} are shown as a function of L for the F and AF configurations with large increase of h at $U_S = 10\Delta$. It is shown that in F configuration, the properties basically keep no change, however, with increasing h, the magnitudes for some peaks and valleys are greatly changed and the number for them become more, stemming from the split of the peaks or valleys. We notice that the spin up (down) EC process can gradually evolve into spin down (up) processes such as at $L = 14$, 15, 31, 35, 48, and 52 (72 and 89). More specifically, with the increase of h, the former disappears gradually, while the latter starts to emerge and then predominate thoroughly. Similarly, as presented above for $L = 31$ (see the left column of Fig. 5), the spin conversion is not changed by the bias voltage eV_L for these SC lengths. This indicates that the tunneling current for some spin direction at these SC lengths can turn into the one for the opposite spin direction, which can be used to produce bipolar spin-conversion diodes. The reason stems from the shift of the energy bands in two ZMRs induced by h as well

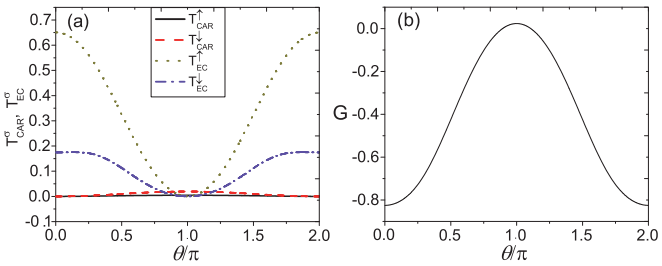

FIG. 8. (a) The CAR and EC transmision probabilities as a function of θ, where $eV_L = -0.7\Delta$, $U_L = U_R = 0$, $h = 5\Delta$, and $U_S = -10\Delta$. (b) The conductances for the same parameters as in (a).

as valley and pseudoparity mixing. In the AF configuration, there are the same properties as those with the less increase of h, i.e., there can exist only CAR processes for the spin up (down) at some SC lengths, for instance, 74 and 91 (96).

C. The noncollinear magnetic configurations

Next, we turn our attention to noncollinear magnetic configurations. In Fig. 8(a), the CAR and EC transmission probabilities as a function of θ are plotted, where $eV_L = -0.7\Delta$, $U_L = U_R = 0$, $h = 5\Delta$, and $U_S = -10\Delta$. Irrespective of θ, $T^{\uparrow}_{\rm CAR} = 0$, indicating that the CAR process is thoroughly prohibited, and $T^{\downarrow}_{\rm CAR} \neq 0$ increases slowly with θ up to π but it is small. With the increase of θ, both $T^{\uparrow}_{\rm EC}$ and $T^{\downarrow}_{\rm EC}$ decrease all the time from $\theta = 0$ to π. Figure 8(b) shows the corresponding conductance for the situation of Fig. 8(a). It is found that the conductance decreases with θ and is not zero at $\theta = \pi$, which just embodies the features of all scattering processes of Fig. 8(a), and could be probed experimentally. In Fig. 9, the conductance versus the SC length L at $\theta = 2\pi/3$ is illustrated. It is noticed that the conductance oscillates with L, being not only positive but also negative. This indicates that at different L, the competition between the EC and CAR processes is characterized by different intensity. For example, the former predominates at $L = 34$, while the latter does at $L = 38$.

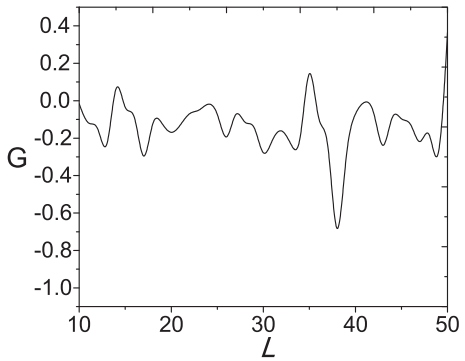

FIG. 9. The conductance vs the SC region length L. Here, $\theta = 2\pi/3$ and other parameters are the same as in Fig. 8(a).

D. Physical origins of the above-obtained features

In the F configuration, due to the valley and pseudoparity mixing in the bulk SC with no valley degree [see Fig. 1(d)], an incident spin-up electron with "+" pseudoparity in the left MZR can propagate into the electronlike (holelike) bands of the SC region. Then the electron enters into the "+" pseudoparity bands of the right MZR but the hole does not because no holelike zero-energy state is involved in the transport for the right ZMR. Hence only the pseudoparity conservation spin-up EC processes are yielded as shown in the left columns of Figs. 6 and 7. However, in the AF configuration, only holelike zero-energy state contributes to the current, therefore there exist the pseudoparity nonconservation spin-up CAR processes (see the right columns of Figs. 6 and 7). The explanations for the existence of the CAR and EC processes with only spin down are given by the same way. Since the electronlike and holelike zero-energy states have opposite pseudoparities for an even MZR at $U_L = 0$ as shown in Fig. 1(c), the AR should be prohibited due to the valley-selection rule.

The oscillation of EC and CAR processes with L are related to the formation of resonant transmission levels inside the SC region due to the presence of two interfaces in the junction. Because the number of channels contributing to the current in the AF is smaller than that in the F, the oscillation of CAR performs more weakly than that of EC does (see Figs. 6 and 7). For SC length L being much smaller than coherent length, the CAR processes hardly have time to take place, and hence the CAR processes are almost suppressed as shown in the right columns of Figs. 6 and 7.

The spin exchange energy causes a shift of the Dirac point from the Fermi level as shown in Fig. 1(c). In the F configuration, for an incident spin-up electron, the channels of zero-energy state of both the left and right MZRs involved in the transport are diminished with the increase of h, leading to the gradual disappearance of spin-up EC process. For an incident spin-down electron, the situation is just contrary (see left columns of Figs. 2–5). In the AF configuration, for an incident spin-up (-down) electron, the channels of zero-energy state of both the left and right MZRs are suppressed with h, thus CAR processes for spin-up and -down disappear gradually (see right columns of Figs. 2–5). In addition, the bias voltage eV_L induces a shift of the Fermi level and resulting variation of the channels of zero-energy state in the left MZR, as a result, different features given by eV_L are exhibited, as shown in Figs. 2–5.

IV. APPLICATION: THE TESTIFICATION OF HELICAL SPIN TEXTURE OF EDGE STATE IN QSHS

QSH insulator is a topological nontrivial phase of electronic matter. Such novel phase is characterized by the gapped bulk states and helical edge states, i.e., the spin-up (spin-down) electrons propagate clockwise (counterclockwise) along the sample edge. Besides the physical significance, the helical states may have important applications in the spintronic device and quantum information processing. Although the edge-state conduction and the spin polarization of the edge current have been confirmed, a direct evidence of the

helical spin texture of edge state remains a challenge [42–49]. Here, we propose to apply the bipolar spin-conversion diode in this work to solve this problem. The proposed setup is shown in Figs. 1(a) and 1(b). The MZR/SC/MZR junction with the bipolar spin-conversion diode function kept at voltages V_L and V_R can be considered as an ensemble, which can supply the incident perfect spin-polarized electrons with the bias voltage bipolarity to the QSH. Under this situation, the MZR/SC/MZR junction and the QSH edge states could be equivalently supposed to be coupled in series. For the F magnetic configuration in the MZR/SC/MZR junction at small h, it can act as a bipolar spin diode with spin up, which at the positive (negative) bias voltage can supply incident spin-up electrons moving from the left (right) lead to the terminal 1 (2) of the QSH. Owing to spin-momentum locking in the QSH, at the positive (negative) V_L, the spin-up electrons move to the right (left) only along the upper (down) edge channels from terminal 1 (2) to 2 (1), finally return to the junction through right (left) lead. However, at large h, the bipolar spin diode turns into the one with spin down. Similarly, due to spin-momentum locking in the QSH, at the positive (negative) V_L, the spin-down electrons move to the right (left) only along the down (upper) edge channels from terminal 1 (2) to 2 (1), finally return to the junction through right (left) lead. Therefore only spin-up (down) current flows in both the QSH and present junction for the positive and negative bias voltages at small (large) h, which can be used to probe and confirm the helical spin texture of the QSH edge states.

V. CONCLUSION

In summary, we propose a zigzag graphene superconducting junction with a bulk SC sandwiched in between two MZRs, directly coupling to the SC, which is characterized by valley and pseudoparity mixing due to the electrons having no valley degree in the bulk SC. It is shown that the two mixings, particularly combined with spin freedom in the MZRs, give rise to novel features for the EC, local AR, and CAR processes in different magnetic configurations. The present setup has the two features: (1) for the F configuration, with the increase of h, there can exist only the EC process for certain spin or with conversion from certain spin to the opposite spin; (2) for the AF configuration, all scattering processes are basically depressed at small L, while there can exist only CAR process for the spin-up or -down regardless of h at large L. Therefore the system can be used to manufacture not only the bipolar spin diode and spin-conversion diode but also the devices with magnetic storage device of high efficiencies and perfect quantum entanglement. In particular, the structure can be combined with the QSH insulator so as to give unambiguous evidence of the helical spin texture in the QSH.

It is pointed out here, although the induction of a magnetic leakage to the s-wave SC near the interface between the MZR and SC is exhibited, it has a weak influence on the SC in general and therefore does not destroy the conductivity as in the usual ferromagnet/SC junctions [50–52]. Thus, our results should be clearly observable in a realistic setup.

ACKNOWLEDGMENTS

This work was supported by the National Natural Science Foundation of China (Grants No. 12274232, No. 11874221, No. 12074332, and No. 12174051), Postgraduate Research & Practice Innovation Program of Jiangsu Province (Grant No. KYCX22_1543), and the Priority Academic Program Development of Jiangsu Higher Education Institutions.

APPENDIX: CALCULATION DETAILS

In Eq. (2), $G^<$ is defined as

$$G^<_{lm,\sigma}(t,t') = i\begin{pmatrix} \langle C^+_{m\sigma}(t')C_{l\sigma}(t)\rangle & \langle C_{m\bar{\sigma}}(t')C_{l\sigma}(t)\rangle \\ \langle C^+_{m\sigma}(t')C^+_{l\bar{\sigma}}(t)\rangle & \langle C_{m\bar{\sigma}}(t')C^+_{l\bar{\sigma}}(t)\rangle \end{pmatrix} \quad \text{(A1)}$$

with $\bar{\sigma} = -\sigma$, $H_{i,i+1}$ and $G^<$ are $8N \times 8N$ matrices by taking both the spin and Nambu spaces into account.

In Eq. (3), the Green's function of the SC region is given by

$$G^r = [E\hat{I} - H_s - \Sigma^L - \Sigma^R - \Sigma^S]^{-1} \quad \text{(A2)}$$

with H_s the Hamiltonian of the SC ribbon region in the Nambu space and $\hat{I}$ a unit matrix. The left and right self-energies $\Sigma^{Lr,Rr}$ can be calculated numerically by the recursive method [53], and that of the SC ribbon region is evaluated by $\Sigma^S = \sum_i t_{l,i} g^r_{Si} t^\star_{i,m}$ with i the same as indices l and m denoting the SC ribbon site. The surface Green's function g^r_{Si} of the SC lead can be transformed from the bulk SC Green's function, particularly for a conventional s-wave SC, they are identical. We assume that each site in the SC ribbon region connects independently a one-dimensional (1D) SC lead as adopted in Ref. [5] for further simplicity, thus the self-energy can be analytically obtained as $\Sigma^S = -ig^S(E\hat{I} + \Delta\hat{\sigma}_x)/2\Omega$, with $\Omega = \sqrt{E^2 - \Delta^2}$ at $|E| > \Delta$ and $\Omega = i\sqrt{\Delta^2 - E^2}$ at $|E| < \Delta$.

[1] A. Rycerz, J. Tworzydlo, and C. W. J. Beenakker, Valley filter and valley valve in graphene, Nat. Phys. **3**, 172 (2007).
[2] A. R. Akhmerov, J. H. Bardarson, A. Rycerz, and C. W. J. Beenakker, Theory of the valley-valve effect in graphene nanoribbons, Phys. Rev. B **77**, 205416 (2008).
[3] A. Cresti, G. Grosso, and G. P. Parravicini, Valley-valve effect and even-odd chain parity in p-n graphene junctions Phys. Rev. B **77**, 233402 (2008).
[4] D. Rainis, F. Taddei, F. Dolcini, M. Polini, and R. Fazio, Andreev reflection in graphene nanoribbons, Phys. Rev. B **79**, 115131 (2009).
[5] J. Wang and S. Liu, Crossed Andreev reflection in a zigzag graphene nanoribbon-superconductor junction, Phys. Rev. B **85**, 035402 (2012).
[6] W. F. Tsai, C. Y. Huang, T. R. Chang, H. Lin, H. T. Jeng, and A. Bansil, Gated silicene as a tunable source of nearly 100% spin-polarized electrons, Nat. Commun. **4**, 1500 (2013).
[7] X. Zhai and G. Jin, Completely independent electrical control of spin and valley in a silicene field effect transistor, J. Phys.: Condens. Matter **28**, 355002 (2016).
[8] Y. Xu and G. Jin, Manipulating topological inner-edge states in hybrid silicene nanoribbons, Phys. Rev. B **95**, 155425 (2017).

[9] C. C. Liu, W. Feng, and Y. Yao, Quantum Spin Hall Effect in Silicene and Two-Dimensional Germanium, Phys. Rev. Lett. **107**, 076802 (2011).

[10] N. Missault, P. Vasilopoulos, F. M. Peeters, and B. Van Duppen, Spin- and valley-dependent miniband structure and transport in silicene superlattices, Phys. Rev. B **93**, 125425 (2016).

[11] Z. P. Niu, Spin-valley filter effect and Seebeck effect in a silicene based antiferromagnetic/ferromagnetic junction, New J. Phys. **21**, 093044 (2019).

[12] X. L. Lü and H. Xie, Bipolar and unipolar valley filter effects in graphene-based P/N junction, New J. Phys. **22**, 073003 (2020).

[13] A. Molle, J. Goldberger, M. Houssa, Y. Xu, S. C. Zhang, and D. Akinwande, Buckled two-dimensional Xene sheets, Nat. Mater. **16**, 163 (2017).

[14] X. C. Zhai, R. Wen, X. F. Zhou, W. Chen, W. Yan, L. Y. Gong, Y. Pu, and X. A. Li, Valley-Mediated and Electrically Switched Bipolar-Unipolar Transition of the Spin-Diode Effect in Heavy Group-IV Monolayers, Phys. Rev. Appl. **11**, 064047 (2019).

[15] Y. J. Wei, T. M. Liu, C. S. Huang, Y. C. Tao, and F. H. Qi, Controllable spin pairing states in silicene-based superconducting hybrid structures with noncollinear magnetizations, Phys. Rev. Res. **3**, 033131 (2021).

[16] Y. Xue, H. Huan, B. Zhao, Y. H. Luo, Z. Y. Zhang, and Z. Q. Yang, Higher-order topological insulators in two-dimensional Dirac materials, Phys. Rev. Res. **3**, L042044 (2021).

[17] S.-R. Eric Yang, M. C. Cha, H. J. Lee, and Y. H. Kim, Topologically ordered zigzag nanoribbon: $e/2$ fractional edge charge, spin-charge separation, and ground-state degeneracy, Phys. Rev. Res. **2**, 033109 (2020).

[18] M. Alidoust, A.-P. Jauho, and J. Akola, Josephson effect in graphene bilayers with adjustable relative displacement, Phys. Rev. Res. **2**, 032074(R) (2020).

[19] M. Alidoust, M. Willatzen, and A.-P. Jauho, Symmetry of superconducting correlations in displaced bilayers of graphene, Phys. Rev. B **99**, 155413 (2019).

[20] M. Alidoust, C. H. Shen, and I. Žutić, Cubic spin-orbit coupling and anomalous Josephson effect in planar junctions, Phys. Rev. B **103**, L060503 (2021).

[21] C. S. Huang, Y. J. Wei, Y. C. Tao, and J. Wang, Spin-orbit coupling assisted magnetoanisotropic Josephson effect in ferromagnetic graphene Josephson junctions, Phys. Rev. B **103**, 035418 (2021).

[22] C. S. Huang, Y. Yang, Y. C. Tao, and J. Wang, Identifying the graphene d-wave superconducting symmetry by an anomalous splitting zero-bias conductance peak, New J. Phys. **22**, 033018 (2020).

[23] J. Linder, M. Zareyan, and A. Sudbø, Spin-switch effect from crossed Andreev reflection in superconducting graphene spin valves, Phys. Rev. B **80**, 014513 (2009).

[24] C. A. Merchant and N. Marković, Electrically Tunable Spin Polarization in a Carbon Nanotube Spin Diode, Phys. Rev. Lett. **100**, 156601 (2008).

[25] F. Qi, Y. Ying, and G. Jin, Thermally driven unipolar and bipolar spin diode based on double quantum dots, J. Appl. Phys. **112**, 084324 (2012).

[26] Y. Wang, Y. Liu, and B. Wang, Graphene spin diode: Strain-modulated spin rectification, Appl. Phys. Lett. **105**, 052409 (2014).

[27] Z. H. Zhang, Y. S. Gui, L. Fu, X. L. Fan, J. W. Cao, D. S. Xue, P. P. Freitas, D. Houssameddine, S. Hemour, K. Wu, and C. M. Hu, Seebeck Rectification Enabled by Intrinsic Thermoelectrical Coupling in Magnetic Tunneling Junctions, Phys. Rev. Lett. **109**, 037206 (2012).

[28] A. Iovan, S. Andersson, Yu. G. Naidyuk, A. Vedyaev, B. Dieny, and V. Korenivski, Spin diode based on Fe/MgO double tunnel junction, Nano Lett. **8**, 805 (2008).

[29] J. P. Eisenstein, L. N. Pfeiffer, and K. W. West, Quantum Hall Spin Diode, Phys. Rev. Lett. **118**, 186801 (2017).

[30] K. Modi, A. Brodutch, H. Cable, T. Paterek, and V. Vedral, The classical-quantum boundary for correlations: Discord and related measures, Rev. Mod. Phys. **84**, 1655 (2012).

[31] L. Aolita, F. de Melo, and L. Davidovich, Open-system dynamics of entanglement: a key issues review, Rep. Prog. Phys. **78**, 042001 (2015).

[32] A. Einstein, B. Podolsky, and N. Rosen, Can Quantum-Mechanical Description of Physical Reality Be Considered Complete?, Phys. Rev. **47**, 777 (1935).

[33] Y. T. Zhang, Z. Hou, X. C. Xie, and Q. F. Sun, Quantum perfect crossed Andreev reflection in top-gated quantum anomalous Hall insulator¨Csuperconductor junctions, Phys. Rev. B **95**, 245433 (2017).

[34] L. Hofstetter, S. Csonka, J. Nygård, and C. Schönenberger, Cooper pair splitter realized in a two-quantum-dot Y-junction, Nature (London) **461**, 960 (2009).

[35] F. H. Qi, J. Cao, and G. J. Jin, Valley-controlled nonlocal transistor based on irradiated and biased bilayer graphene, Phys. Rev. B **98**, 045422 (2018).

[36] J. Wang, L. Hao, and K. S. Chan, Quantized crossed-Andreev reflection in spin-valley topological insulators, Phys. Rev. B **91**, 085415 (2015).

[37] L. Hofstetter, S. Csonka, A. Baumgartner, G. Fülöp, S. d'Hollosy, J. Nygård, and C. Schönenberger, Finite-Bias Cooper Pair Splitting, Phys. Rev. Lett. **107**, 136801 (2011).

[38] L. G. Herrmann, F. Portier, P. Roche, A. L. Yeyati, T. Kontos, and C. Strunk, Carbon Nanotubes as Cooper-Pair Beam Splitters, Phys. Rev. Lett. **104**, 026801 (2010).

[39] Z. Hou, Y. Xing, A.-M. Guo, and Q. F. Sun, Crossed Andreev effects in two-dimensional quantum Hall systems, Phys. Rev. B **94**, 064516 (2016).

[40] W. Chen, R. Shen, L. Sheng, B. G. Wang, and D. Y. Xing, Resonant nonlocal Andreev reflection in a narrow quantum spin Hall system, Phys. Rev. B **84**, 115420 (2011).

[41] T. M. Liu, F. J. Chen, Y. C. Tao, and C. S. Huang, Perfect modulation between fully spin-polarized spin-singlet and-triplet Andreev entanglements in a narrow quantum spin Hall system, Europhys. Lett. **132**, 37001 (2020).

[42] C. Y. Hou, E. A. Kim, and C. Chamon, Corner Junction as a Probe of Helical Edge States, Phys. Rev. Lett. **102**, 076602 (2009).

[43] T. L. Schmidt, Current Correlations in Quantum Spin Hall Insulators, Phys. Rev. Lett. **107**, 096602 (2011).

[44] J. M. Edge, J. Li, P. Delplace, and M. Büttiker, $\mathbb{Z}_2$ Peak of Noise Correlations in a Quantum Spin Hall Insulator, Phys. Rev. Lett. **110**, 246601 (2013).

[45] F. Romeo and R. Citro, Interaction effects in nonequilibrium transport properties of a four-terminal topological corner junction, Phys. Rev. B **90**, 155408 (2014).

[46] S. Das and S. Rao, Spin-Polarized Scanning-Tunneling Probe for Helical Luttinger Liquids, Phys. Rev. Lett. **106**, 236403 (2011).

[47] A. Soori, S. Das, and S. Rao, Magnetic-field-induced Fabry-Pérot resonances in helical edge states, Phys. Rev. B **86**, 125312 (2012).

[48] K. Luo, W. Chen, L. Sheng, and D. Y. Xing, Random-Gate-Voltage Induced Al'tshuler-Aronov-Spivak Effect in Topological Edge States, Chin. Phys. Lett. **38**, 110302 (2021).

[49] W. Chen, W. Y. Deng, J. M. Hou, D. N. Shi, L. Sheng, and D. Y. Xing, π Spin Berry Phase in a Quantum-Spin-Hall-Insulator-Based Interferometer: Evidence for the Helical Spin Texture of the Edge States, Phys. Rev. Lett. **117**, 076802 (2016).

[50] A. A. Golubov, M. Yu. Kupriyanov, and E. Il'ichev, The current-phase relation in Josephson junctions, Rev. Mod. Phys. **76**, 411 (2004).

[51] A. I. Buzdin, Proximity effects in superconductor-ferromagnet heterostructures, Rev. Mod. Phys. **77**, 935 (2005).

[52] F. S. Bergeret, A. F. Volkov, and K. B. Efetov, Odd triplet superconductivity and related phenomena in superconductor-ferromagnet structures, Rev. Mod. Phys. **77**, 1321 (2005).

[53] M. P. López Sancho, J. M. López Sancho, and J. Rubio, Highly convergent schemes for the calculation of bulk and surface Green functions, J. Phys. F: Met. Phys. **15**, 851 (1985).